materials

MDPI

Review

Piezoelectric Charge Coefficient of Halide Perovskites

Raja Sekhar Muddam, Joseph Sinclair and Lethy Krishnan Jagadamma *

Energy Harvesting Research Group, School of Physics & Astronomy, Scottish Universities Physics Alliance (SUPA), University of St Andrews, North Haugh, St Andrews KY16 9SS, UK; rsm22@st-andrews.ac.uk (R.S.M.); js450@st-andrews.ac.uk (J.S.)
* Correspondence: lkj2@st-andrews.ac.uk

Abstract: Halide perovskites are an emerging family of piezoelectric and ferroelectric materials. These materials can exist in bulk, single-crystal, and thin-film forms. In this article, we review the piezoelectric charge coefficient (d_{ij}) of single crystals, thin films, and dimension-tuned halide perovskites based on different measurement methods. Our study finds that the (d_{ij}) coefficient of the bulk and single-crystal samples is mainly measured using the quasi-static (Berlincourt) method, though the piezoforce microscopy (PFM) method is also heavily used. In the case of thin-film samples, the (d_{ij}) coefficient is dominantly measured by the PFM technique. The reported values of d_{ij} coefficients of halide perovskites are comparable and even better in some cases compared to existing materials such as PZT and PVDF. Finally, we discuss the promising emergence of quasi-static methods for thin-film samples as well.

Keywords: halide perovskite thin films; quasi-static measurements; d_{33} coefficient; halide perovskite crystals; 2D-perovskites

Citation: Sekhar Muddam, R.; Sinclair, J.; Krishnan Jagadamma, L. Piezoelectric Charge Coefficient of Halide Perovskites. *Materials* **2024**, *17*, 3083. https://doi.org/10.3390/ma17133083

Academic Editors: Lorena Pardo, Sebastiano Garroni, Laura Stoica and Sandy Cochran

Received: 19 May 2024
Revised: 14 June 2024
Accepted: 19 June 2024
Published: 23 June 2024

1. Introduction

Ambient energy harvesting has always garnered research attention as an alternative and sustainable powering method to meet our ever-increasing energy demand [1–3]. The anticipated future technological advancements such as the Internet of Things, wearables, and the international efforts to tackle the climate crisis (Net-Zero 2050) have led to unprecedented global research attention to the various ambient energy harvesting methods. Ambient energy harvesting refers to the energy conversion processes in which different forms of energy available in our surroundings (mostly wasted forms) are converted to a usable form of electricity [4,5]. Depending on the scale of harvestable energy, these electricity generation processes are classified as (a) microscale and (b) macroscale energy harvesting. In macroscale energy harvesting, large-scale sources such as sunlight, water flow, ocean waves, heat from the sun, wind, and the motion of large automotive vehicles such as trains, trucks, etc., are considered. In the case of microscale energy harvesting, the harvestable energy sources are relatively low-power, such as ambient light inside buildings, electromagnetic waves such as RF, vibrations from household appliances and industrial equipment, human walking, human movements, air-flow movements in HVAC systems etc. [6,7]. Ambient energy harvesting uses different physical phenomena such as the photovoltaic effect, electromagnetic induction, thermo-electric effect, pyroelectricity, piezoelectricity, triboelectricity, and magnetostriction in generating useful forms of electricity. Among these, the present review is particularly focussed on mechanical energy harvesting using the piezoelectric method with a particular emphasis on its application in the Internet of Things (IoT) [3].

The IoT is a smart network of internet-connected electronic and electrical devices that can communicate with each other and respond rapidly in real time. It is considered as the technology linking and integrating the digital and physical world. In the next 10–15 years, the number of connected devices in the IoT is predicted to range from 75 billion to more

than 1 trillion [8]. Wireless sensors are the most fundamental components in the IoT, and they should have the ability to operate for long periods for continuous process monitoring and data transfer. Currently, they are mainly powered by batteries, and this reliance on batteries causes service interruptions, limits the functionality and deployability of IoT systems, and is not a practical powering method when these technologies have grown to their full potential (200 million battery replacements per day), and poses an environmental challenge due to the disposal of dead batteries as well [9]. Hence, the development of alternate powering methods other than batteries and wired power supply from the electrical grid is necessary for these wireless sensor platforms in the IoT. The self-powering of these wireless sensor platforms using ambient energy harvesters bestows them the ability to be functional for long periods autonomously [10,11].

Among the various ambient energy harvesting technologies available, photovoltaics and piezoelectricity are particularly significant because of the high density of harvestable ambient energy available (100 mW/cm^2 for sunlight and 800 $\mu W/cm^3$ for piezoelectricity) [12] and the high efficiency of the conversion to electrical power. State-of-the-art photovoltaic devices are capable of converting light to electricity with a 25% conversion efficiency, and within the last 30 years, several new photovoltaic materials other than the debut silicon solar cells have also emerged, such as CdTe, CIGS, DSC, organic PVs, and halide perovskites [13]. However, a similar comparison to the development of piezoelectric materials shows that the materials widely in use for commercial applications are still the ones developed in the 1970–1980s such as PZT, $BaTiO_3$, etc.

Piezoelectric materials convert mechanical energy to electrical energy by developing a dipole moment in them when mechanical stress is applied, and, vice versa, they become deformed when an electrical energy is applied. Our interest in piezoelectricity is based on two aspects: (a) it can be considered for both macro- and microscale energy harvesting since the harvestable sources are available in both ranges in the ambient environment and (b) the necessity of developing newer piezoelectric materials and fabrication methods to advance this technology further as the existing materials such as Barium Titanate and lead zirconate suffer from brittleness, lack of flexibility, and conformability, require high-temperature and high-pressure processing, and are usually bulky [14].

Recently, halide perovskites have been reported to possess promising piezoelectric properties in addition to their photovoltaic properties [15,16]. Hybrid halide perovskites are a family of materials that bind organic and inorganic components to a molecular composite. These materials are represented by a general chemical formula of ABX_3, where A is an organic or inorganic cation, B is a divalent cation, such as Pb^{2+} or Sn^{2+}, and X is a halogen, such as I^-, Br^-, or Cl^- (Figure 1a). Organic cations, A, can be methylammonium (MA) $CH_3NH_3^+$, ethylammonium (EA) $C_2H_5NH_3^+$, formamidinium (FA) $HC(NH_2)_2^+$, and even inorganic Cs [17,18]. The molecular structure of the hybrid perovskite metal halides consists of a three-dimensional (3D) metal halide framework, which encapsulates the polyatomic organic cations. The motion of the organic cations with large dipole moments in the metal halide cavity gives rise to unusual electrical properties in hybrid perovskites. This dipole moment (μ) is related to the symmetry of the organic cation, such as $\mu MA^+ >> \mu\ FA^+ > \mu\ GA^+ \sim 0$, where $MA^+ = CH_3NH_3^+$ $FA^+ = HC(NH_2)_2^+$ $GA^+ = C(NH_2)_3^+$ [19].

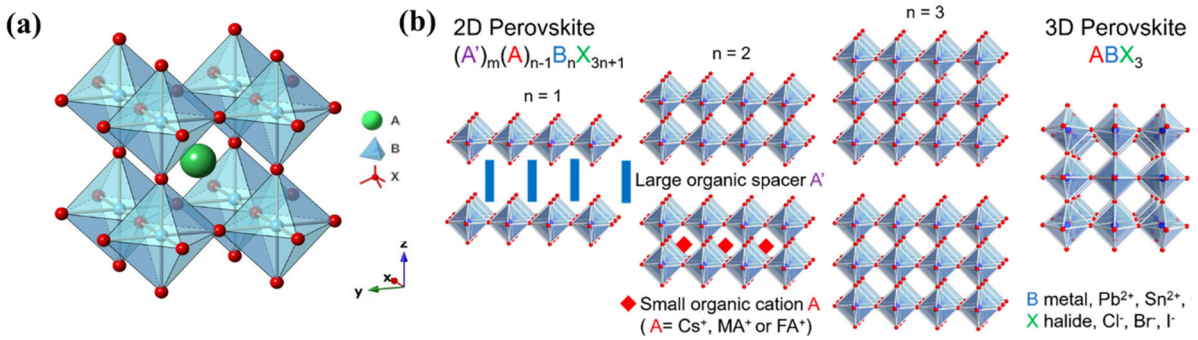

Figure 1. (**a**) Three-dimensional halide perovskite with the chemical formula ABX_3 [20]. (**b**) Schematic illustration of the evolution from 2D perovskite to 3D perovskite with key components. Reproduced with permission from Ref [21].

Low-dimensional halide perovskites (general formula $R_2A_{n-1}B_nX_{3n+1}$) (Figure 1b) are also emerging as promising piezoelectric materials where the polarisation originates mainly from the contribution from the A cation as well as the symmetry breaking from the longer R cation [22,23]. Based on the symmetry, the hybrid perovskites can be classified as centrosymmetric, asymmetric, and non-centrosymmetric. Moreover, the degree of non-centrosymmetry can be tuned by applying an external stimulus of heat, electric field, photon energy, stress, etc. [10]. This tuning of non-centrosymmetry gives rise to many interesting properties of piezoelectric, pyroelectric, and high switchable dielectric constants in halide perovskites. Since halide perovskites are emerging as an important piezoelectric material to realise milli–microwatt power-generating devices, it is high time to consolidate the d_{33} coefficients reported for this family of materials in their bulk (crystals and powders) and thin-film formats and the methods routinely being used for these measurements. This review article is mainly focussed on the piezoelectric charge coefficient (d_{33}) of various families of halide perovskites such as (a) 3D and (b) low-dimensional halide perovskites (2D and 1D).

2. Piezoelectric Charge Coefficient (d_{33})

While developing new piezoelectric materials, one of the most important parameters to consider is its piezoelectric coefficient (d_{ijk}) or the charge coefficient. Depending on the direct (mechanical to electrical) or converse piezoelectric effect (electrical energy to mechanical strain), the charge coefficients are defined as follows:

$$d_{ij} = \frac{charge\ produced}{Applied\ stress}$$

$$d'_{ij} = \frac{strain\ produced}{Applied\ voltage}$$

Associated with the d_{ij} coefficient is the corresponding voltage coefficient g as well. Its definition is as follows:

$$g = \frac{Electric\ field\ developed}{Applied\ Mechanical\ stress} = \frac{E}{T}$$

The relation between the charge coefficient (d_{ij}) and the voltage coefficient (g) is as follows:

$$d = \varepsilon g$$

When developing efficient mechanical energy harvesters, the efficiency of energy conversion is denoted by a parameter known as the coupling coefficient, k [24].

$$k^2 = \frac{stored\ mechanical\ energy}{input\ electrical\ energy} = \frac{stored\ electrical\ energy}{input\ mechanical\ energy}$$

The value of k ranges from 0 to 1. k is related to the d_{33} coefficient as follows:

$$k^2 = dgY$$

where Y is the Young's modulus.

So, to have a higher coupling coefficient, the d_{33} coefficient needs to be higher.

In addition to this, the stored electrical energy per unit volume is also directly proportional to the square of the d coefficient.

$$U_{ele.stored/volume} = \frac{1}{2}\frac{d^2T^2}{\varepsilon_0\varepsilon_r}$$

where T is the applied stress. In this review, we mainly focus on the d_{33} coefficients of the halide perovskites where the direction of the polarisation and the applied stress are along the same axis.

3. Measurement Methods of Piezoelectric Charge Coefficient (d_{33})

The existing methodologies for the d_{33} measurements are briefly summarised below:

1. Quasi-static (Berlincourt method);
2. Dynamic resonance;
3. Laser interferometry;
4. Piezoforce microscopy (PFM).

3.1. Quasi-Static Measurement Method for d_{33} Coefficient

The term quasi-static means the measurements are conducted slowly enough (almost statistically) at low frequencies so that the d_{33} values are measured under equilibrium conditions. The quasi-static measurement of the d_{33} coefficient is also widely known as the Berlincourt method after Don Berlincourt, who devised the first commercial d_{33} meter based on the principle of the quasi-static method.

To understand the principle of the QS method, starting with the basic (direct) piezoelectric relationship is useful:

$$D = \varepsilon^T E + dT \quad (1)$$

where D is the electric displacement, d is the piezoelectric charge (strain) coefficient depending on the direct (converse) piezoelectric effect expressed in C/N or pm/V, ε^T is the dielectric permittivity under constant stress conditions, and T is the stress expressed in N/m^2.

When no external electric field E is applied or the field is very small, Equation (1) can be written as

$$D = dT \quad (2)$$

Here, D is expressed in C/m^2 and T in N/m^2. By rewriting the above equation, the following is found:

$$d = [\left(\frac{Q}{A}\right) \div \left(\frac{F}{A}\right)] = Q/F \quad (3)$$

where Q is the charge developed due to an applied force F and A is the active area. This equation shows that the d_{33} coefficient can be obtained by measuring the charge generated along the polar direction (z-direction in this case) in response to a force applied along the same direction.

In the original 'static' method, as reported by Jaffe et al., two weights (to apply force) and a capacitor with a large capacitance can be used for the d_{33} measurement [25]. One weight (considered as the 'dead weight' and the bias force) and the shunt capacitor (connected in parallel or across with the piezo material for which the d_{33} measurement is needed) together will satisfy the boundary condition of zero electric field. Then, the second weight is applied/removed, and the transient voltage across the shunt capacitor due to the applied force bias (stress) can measure the charge developed on the DUT. From this, one can estimate the d_{33} coefficient of the device under test. The voltage developed during the introduction and removal of the second weight should match the same change in stress. Even though this static method is simple, the reliability is low due to the high possibility of external static charge involvement, charge generation due to the pyroelectric effect, and thermal drift, and in the case of ferroelectric-type samples, the neglection of D/E can further mislead the d_{33} value measured as the electric boundary conditions are violated [25–27].

The quasi-static method was developed to overcome the shortcomings of the application of a static load and eliminate the drift due to the pyroelectric charge. In the quasi-static measurements, a low-frequency oscillating and small-magnitude mechanical force is applied, and the corresponding charge output is measured. The charge developed is then divided by the magnitude of applied force to obtain d_{33}. Here, the measurements are performed at a few hundred hertz, and this should be below the resonant frequency of the system so that the same formula as applied to the static cases is still applicable [27].

The small oscillating force is applied using a loudspeaker-type coil. The upper (1 KHz) and lower (10 Hz) limit of the frequency of the applied force is, respectively, determined by the mechanical resonance of the force-head unit and thermal drift. The DUT and the reference sample (usually) PZT are connected along the same line of action of force (Figure 2a) so that the same force is applied to the sample as well as the reference sample. To avoid the rattling of the sample and to keep it stable during the measurement, a static pre-load is usually applied. Knowing the capacitance and the d_{33} coefficient of the reference sample and the high sensitivity of the reference sample allows for the measurement of the force applied. The DUT and the reference sample electrical connections are typically as shown in Figure 2a. The constant field or short-circuit condition is achieved by connecting a large capacitor across the DUT (shunt capacitor) or by using a virtual earth amplifier. The d_{33} coefficient can then be determined by measuring the charge across the sample and reference or by taking the ratio of the respective voltages. In the latter case, taking the ratio of the voltage or (charge) across the sample to the reference gives the d_{33} coefficient.

To ensure that the d_{33} coefficient is measured under equilibrium conditions or with the minimum error, attention needs to be paid to the input parameters such as the static pre-load, magnitude and frequency of the oscillating force applied, time-dependent effects, and proper calibration of the measurement system. The magnitude of the oscillating force is usually of the order of 0.1 N, and this relatively low force ensures that the DUT is in the linear regime (the charge produced is linear to the force). The frequency of the oscillating force field is usually 100 Hz, as above this and towards 1 kHz, there is interference from the resonance of the force head. Depending on the soft or hard piezoelectric materials, a response below 100 Hz can be frequency-dependent and is purely material-dependent. The low-frequency limit of 10 Hz is usually set by the thermal drift and the static charge dissipation to the surroundings. The purpose of the pre-load is to hold the sample in place and to establish the zero-field boundary conditions so that it does not move during the oscillating force. The range within which d_{33} values remain stable is typically below 10 N.

3.2. Dynamic Resonance Method

The dynamic resonance method is also known as the frequency method, resonance–antiresonance, and double resonance method. This method can give a complete matrix of the material coefficients, such as the elastic compliance constants (S_{ij}), piezoelectric voltage and charge constants (g_{ij} and d_{ij}), electromechanical coupling (k_{ij}) coefficient, capacitance,

and dielectric constant [28,29]. This method works by the principle of natural and resonant frequency of samples of different sizes and shapes. The resonant frequency of a sample corresponds to the frequency of vibration of a system (electrical or mechanical in this context) at which it gives the maximum oscillatory response corresponding to an external excitation condition, and it happens when the external driving frequency matches with the natural frequency of the sample under test [27]. To conduct measurements using this method, an alternating electrical signal is applied at the ends of the piezoelectric sample, and the frequency of the excitation signal is swept by keeping its amplitude the same (reverse piezoelectric effect). At the resonance condition, the real part of the admittance becomes maximum, and the imaginary part is close to zero. This method is easier to understand considering the equivalent circuit of a piezoelectric device which consists of a parallel connection of static capacitance (one branch) and another branch representing the dynamic part (a series connection of L, C, and R), as shown in Figure 2b [27,28,30]. Depending on the sample geometry, a variety of vibration modes is possible by inducing resonance effects in different directions. There are recommended sample geometries for exciting the various modes [27]. An impedance analyser is used to carry out this measurement, and the admittance circle will give information about the series and parallel resonant frequencies f_s and f_p, the resonant frequency f_r, antiresonant frequency f_a, maximum impedance frequency f_{max}, and minimum impedance frequency f_{min}, which in turn can be employed to extract the main tensor matrix component of the material coefficients of the piezoelectric crystal in vibration mode [28,29]. The disadvantage of this method is the requirement of samples of different shapes such as disc, plate, and cylinder with certain aspect ratios to extract the complete matrix coefficients.

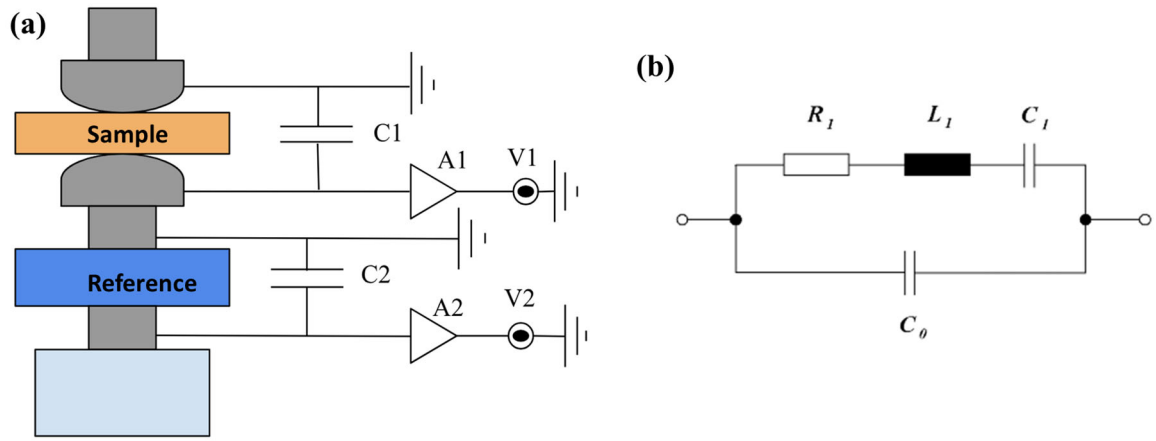

Figure 2. (**a**) Schematic of the Berlincourt method; (**b**) equivalent circuit of a piezoelectric transducer [31].

3.3. Laser Interferometry Method

Like the resonance–antiresonance method, the laser interferometry method also uses the reverse piezoelectric effect. In this method, after the application of a polarisation voltage, the nano–microrange of displacements generated through the piezoelectric effect is measured through high-resolution laser interferometry [27,29]. This method allows for the measurement of piezoelectric charge coefficients, without mechanical contact, and a thin-film expansion with a measurement resolution much better than 1 pm is possible. However, the method requires high accuracy in the construction and isolation of the measurement system from the parasitic vibration [32].

In a typical Michelson interferometer, for the measurement of the piezocoefficient, a reference and a probe beam constituted by a monochromatic wavelength λ are made to

interfere, and the intensity of this interfering light beam is measured. The interference light intensity is given by the following:

$$I = \left|E_{p(t)} + E_{r(t)}\right|^2 = I_p + I_r + 2\sqrt{I_p I_r}\, cos\left(\frac{4\pi\Delta d}{\lambda}\right)$$

where I_p and I_r are the intensities of the probing and reference beams. Δd is the optical path length difference between two beams [33]. The optical path length Δd is related to the sample displacement. Corresponding to this displacement, an amplified output voltage signal is produced. The interferometry sensitivity parameter (IFS) is set to a specific value based on the displacement/unit volume (such as 10 nm/V or 50 nm/V). Using these parameters, the charge coefficient d_{33} is calculated using the following relation [32]:

$$d_{33} = \frac{\Delta l}{V_{in}} = \frac{IFS \times \Delta V}{V_{in}}$$

where Δl is the displacement, V_{in} the input voltage, IFS is the spectral sensitivity, and ΔV is the voltage.

3.4. Piezoforce Microscopy (PFM)

PFM is used to study the piezo and ferroelectric properties of the materials at the nanoscale, and it measures the nanoscale topography simultaneously with the electromechanical coupling (d_{33}^{eff}) in response to an electrical signal.

It works based on the converse piezoelectric effect (Figure 3), and here, the voltage signal is applied to the sample and measures its mechanical extension at the nanoscale.

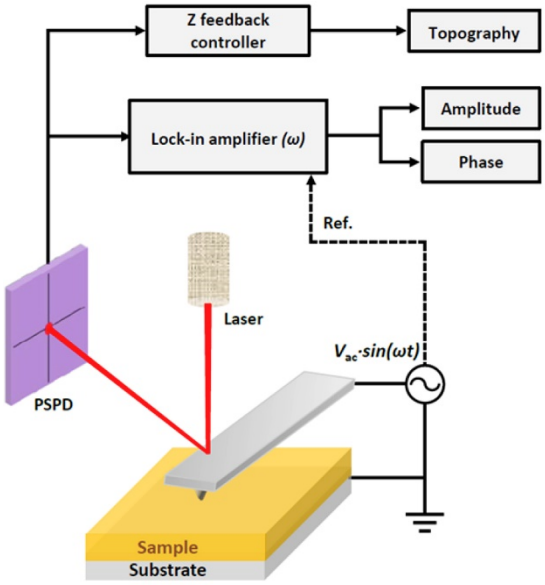

Figure 3. Working principle of piezoforce microscopy. Adapted from Ref [34].

The converse piezoelectric coefficient is $d_{33}^{eff} = \frac{\text{displacement (pm)}}{\text{applied voltage (V)}} = \frac{dS}{dV}$.

This technique is an alternate version of contact-mode Atomic Force Microscopy (AFM), and here, the AFM tip is in contact with the sample surface. PFM is used for topography imaging; it falls under the derivative imaging mode, and it is derivative of primary imaging.

In PFM, the tip is conductive; here, an electrical signal is applied between the piezoelectric sample and tip. The applied electric field-induced mechanical strain response is associated with surface deformation, which reflects on surface topography. The lock-in

amplifier compares the applied input signal $V_{in} = A\cos(\omega t + \varphi)$ to the reference signal $V_{ref} = B\cos(\omega t)$, which are multiplied together to obtain a demodulation output.

$$V_{out} = \frac{1}{2}AB\cos(\varphi) + \frac{1}{2}AB\cos(2\omega t + \varphi)$$

Here, A and B are input and reference signal amplitudes; ω, φ is the frequency and phase of both the input and reference signals. From this amplifier output, finally, the phase and amplitude images of the resultant piezoelectric sample are extracted.

The number of publications detailing the piezoelectric properties of halide perovskites is increasing rapidly, as shown in Figure 4. In the subsequent sections, the d_{ij} coefficient of halide perovskites is summarised based on the sample format, such as thin films and crystals, and the measurement method, as depicted above. Since the Curie temperature (T_c) is critical in identifying the various functional applications and enhanced power handling capacity of ferroelectric and piezoelectric materials and their integration with modern electronics, this information is included for the halide perovskites while listing the d_{33} values whenever this information is available.

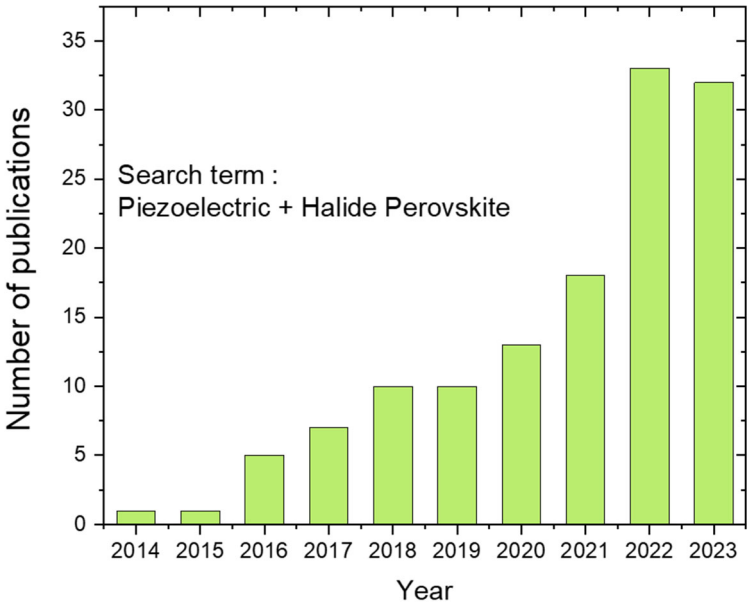

Figure 4. A graph showing the number of halide perovskite-based piezoelectric-related publications as a function of year.

4. d_{33} Coefficients of Halide Perovskites

4.1. d_{33} Coefficients of Halide Perovskite Crystals

Table 1 lists the d_{33} coefficients reported for the halide perovskite crystals. Recently, Zhao et al. reported a piezoelectric coefficient of 7 pC/N for $MAPbI_3$ single crystals measured using a custom-made d_{33} meter. The ferroelectricity in $MAPbI_3$ is attributed to the order–disorder transition of the MA^+ cation, and it has a Curie temperature of 58 °C [35]. A slightly higher piezoelectric coefficient of 10.81 pV/m has been reported for $MAPbI_3$ single crystals using PFM measurement. These $MAPbI_3$ crystals also demonstrated pressure-induced enhancement in the photodetection properties, i.e., the piezo–phototronic effect [36]. Light-induced enhancement in the piezocoefficient from 2.0 to 4.31 pC/N as measured through the quasi-static method has been reported for $MAPbBr_3$ single-crystal samples [37]. The light source used was a 405 nm laser with a power density of ~ 200 mW/cm^2. A consistently higher d_{33} coefficient >10 pC/N measured by the quasi-static method has been observed for $FA_xMA_{1-x}PbI_3$ (x = 0–0.1) single crystals [38]. A light-intensity-dependent d_{33} coefficient has been reported for thin $MAPbBr_3$ single crystals. The d_{33} coefficient measured using custom-built d_{33} meter working on the principle of the

quasi-static method increased from 20 pC/N to 87 pC/N as the light intensity increased from 4 mW/cm^2 to 100 mW/cm^2 [39]. A large d_{33} coefficient of 137 pC/N measured using the quasi-static method has recently been reported in a vacancy-ordered double halide perovskite (with the structural formula A_2BX_6) of $TMCM_2SnCl_6$ crystals where TMCM represents trimethylchloromethylammonium. In addition, 50% $[SnCl_6]^{2-}$ octahedrons are replaced by periodic vacancies in piezoelectric $TMCM_2SnCl_6$ in which the asymmetric $TMCM^+$ takes the A sites [40]. The origin of piezoelectricity is attributed to the halogen-bond-mediated united movement of atomic displacement in $[SnCl_6]^{2-}$ octahedrons and the molecular rotation of the A cation $TMCM^+$.

A molecular ferroelectric and semiconducting 2D halide perovskite of (4-amino tetrahydropyran)$_2PbBr_4$ [$(ATHP)_2PbBr_4$] crystals has recently been reported as a promising piezoelectric material with a high piezoelectric d_{33} coefficient of 76 pC/N, as measured using the piezoforce microscopy (PFM). This material has a high Curie temperature of 503 K, higher than the conventional oxide perovskite of Barium Titanate [41]. Using the Berlincourt method, a large d_{33} coefficient of 1540 pC/N was obtained for the molecular ferroelectric solid solution with a morphotropic phase boundary (MPB) for the composition range ($0 \leq x \leq 1$) $(TMFM)_x(TMCM)_{1-x}CdCl_3$ (TMFM, trimethylfluoromethyl ammonium; TMCM, trimethylchloromethyl ammonium) [42]. This high d_{33} coefficient is attributed to the existence of a morphotropic phase boundary (MPB) of monoclinic and hexagonal phases for this particular composition. Previously, the MPB between the ferroelectric tetragonal and rhombohedral phases was reported for conventional oxide perovskites such as PZT leading to its high d_{33} of ~590 pC/N for a 52/48 Zr/Ti ratio [26,43]. However, it is worth noting that the investigation of MPB in halide perovskites is in its very infancy. It is highly promising to note that a series of pb-free halide perovskite molecular ferroelectric crystals with TMCM, trimethylchloromethyl ammonium, as the A cation has shown d_{33} values ranging from 100 to 500 pC/N, comparable to that of conventional PZT, attracting research attention [44]. However, Chen et al. have noted that by introducing Br into TMCMC-$CdCl_3$, it is possible to soften the lattice and simultaneously obtain a large voltage and charge coefficient. Thus, the authors reported a high d_{33} value of 440 pC/N measured using the quasi-static method and a g_{33} value of 6215×10^{-3} Vm/N [45]. Using the design principle of homochirality, Yang et al. designed piezoelectric and ferroelectric 2D perovskites of [R- and S-1-(4-Chlorophenyl)ethylammonium]$_2PbI_4$ with a d_{33} coefficient of 3 pm/V measured using PFM. These materials showed a bandgap of ~2.3 eV and good absorption in the visible spectral range [46]. Using DFT calculations, a one-dimensional enantiomorphic hybrid metal halide R/SMP$CdCl_4$(R/SMP = R/S-2-methylpiperazine) with chiral properties was predicted to have high piezoelectric constants (16.71, 8.39, and 7.35 pC/N) [47]. By introducing chiral and rigid organic cations of α-phenylethylammonium, *R*-α-PEA$^+$, and *S*-α-PEA$^+$ into bismuth-based hybrid halides, chiral (*R*-α-PEA)$_4Bi_2I_{10}$ and (*S*-α-PEA)$_4Bi_2I_{10}$ crystals (centimetre-sized single crystals) were formed to yield an enhanced piezoelectric coefficient d_{22} of 32 pC/N, as measured using the quasi-static method [48].

Halogenobismuthates(III) with a piezoelectric effect are rarely reported. Recently, semiconducting and piezoelectric crystals of trimethylsufonium bismuth bromide $[(CH_3)_3S]_3[Bi_2Br_9]$ with a d_{33} coefficient of 18 pC/N measured using the quasi-static method were reported by Zhang et al. [49]. New hybrid lead-free metal halide $(BTMA)_2CoBr_4$ (BTMA = benzyltrimethylammonium) crystals with normal and shear piezoelectric responses (d_{22} and d_{25}) of 5.14 and 12.4 pC/N, respectively, and with a non-perovskite crystal structure were synthesized by Guo et al. [50] In addition to the conventional octahedral perovskite structures (ABX_3) mostly investigated, tetrahedral perovskites with the general formula (AM_2X_5) (A is a cation, M = Pb or Sn, and X = Cl, Br, or I) also seem to be promising for exploring the piezoelectric properties. Recently, Sahoo et al. reported a d_{33} coefficient of 72 pm/V for $CsPb_2Br_5$ microplates measured using the PFM method [51]. Single crystals of metal-free halide perovskite of N-methyl-N′-diazabicyclo [2.2.2] octonium–ammonium triiodide (MDABCO-NH4I_3) have recently been reported to possess a d_{33} coefficient of 12.8 pm/V using the PFM method, and the promising potential of these materials for

wearable applications were also demonstrated [52]. Halide double perovskites having a general formula of $A_2B^+B^{3+}X_6$ or $A_2B^{4+}X_6$ (A = MA or Cs; B = Pb, Sn, Cu, or Bi; X = Cl, Br, or I) possess tuneable optoelectronic properties and better air stability compared to 3D halide perovskites. A comparison with three different Pb-halide-based and Sn-halide-based double perovskites showed negative d_{33} coefficients of MA_2SnCl_6 (d_{33} = −32.51 pC/N), MA_2SnBr_6 (−9.00 pC/N), and MA_2SnI_6 (−7.97 pC/N). These values were estimated using DFT calculations. The study also showed an increasing trend of d_{33} values with the size reduction in the halogen ions [53]. In contrast to this observation, an increasing piezoelectric response with an increase in halogen size was recently predicted using DFT calculations for $CsGeX_3$ (X = Cl, Br, and I) as 0.731, 1.829, and 12.48 C m^{-2} for X = Cl, Br, and I, respectively [54].

Table 1. List of d_{33} coefficients of halide perovskite crystals and the measurement method used. The Curie temperature (T_c) is also included in the case of molecules for which this information was available.

Halide Perovskite Composition	d_{ij} Coefficient (d_{33} Unless Mentioned)	Measurement Method	Curie Temperature Tc(°C)	Reference
$MAPbI_3$	7 pC/N	Quasi-static	58	Ref [35]
$MAPbI_3$	10.81 pm/N	PFM		Ref [36]
$FA_xMA_{1-x}PbI_3$ (x = 0–0.1)	10 pC/N	Quasi-static		Ref [38]
$MAPbBr_3$	20 pC/N	Quasi-static		Ref [39]
$TMCM_2SnCl_6$	137 pC/N	Quasi-static	92	Ref [40]
$(ATHP)_2PbBr_4$	76 pC/N	PFM	230	Ref [41]
$(TMFM)_x(TMCM)_{1-x}CdCl_3$ ($0 \leq x \leq 1$)	1540 pC/N	Quasi-static	100	Ref [42]
TMCMC-$CdCl_3$,	440 pC/N	Quasi-static	100	Ref [45]
[R- and S-1-(4-Chlorophenyl)ethylammonium]$_2PbI_4$	3 pm/V	PFM		Ref [46]
(*R*-α-PEA)$_4Bi_2I_{10}$ and (*S*-α-(PEA)$_4Bi_2I_{10}$	32 pC/N (d_{22})	Quasi-static	197	Ref [48]
$[(CH_3)_3S]_3[Bi_2Br_9]$	18 pC/N	Quasi-static	25	Ref [49]
$(BTMA)_2CoBr_4$	d_{22} 5.14 pC/N d_{25} 12.4 pC/N	Quasi-static		Ref [50]
$CsPb_2Br_5$	72 pm/V	PFM		Ref [51]
MDABCO-NH4I_3	12.8 pm/V	PFM	90	Ref [52]

4.2. d_{33} Coefficients of Halide Perovskite Thin Films

Table 2 lists the d_{33} coefficients of halide perovskite thin films and the measurement method used. The first report on the d_{33} coefficients of halide perovskites was published in 2015 by Juan Bisquert et al. Using the PFM method, the d_{33} of $MAPbI_3$ was measured to be 5 pm/V, which then increased to 25 pm/V upon white light illumination [55]. The incorporation of Fe^{2+} to partially replace Pb^{2+} has been found to profoundly enhance the d_{33} coefficient of $MAPbI_3$ from 5 pm/V to 17.5 pm/V, as measured through PFM [56]. A comparison of the piezoelectric coefficient of $MAPbI_3$ polycrystalline films on different substrates showed that by interfacing $MAPbI_3$ thin films with PZT substrates the d_{33} coefficient measured using the PFM method enhanced from 0.3 pm/V to 4 pm/V by aligning the dipole moment of the MA cation [57]. Kim et al. reported the first all-inorganic and multilayered (with Cu metal) $CsPbI_3$ thin films with a d_{33} coefficient of 15 pm/V measured using the PFM method [58]. After the poling process, the d_{33} value of the

multilayered structure improved to 30 pm/V. Strain engineering has been successfully used by Kim et al. for $CsPbBr_3$ films to modify the d_{33} coefficient from 9.3 pm/V for 0.75% tensile strain to 23.2 pm/V for a compressive strain of an equal amount [59]. A similar strain engineering mechanism has been applied to hybrid organic–inorganic thin films of $MAPbI_3$, $MAPbBr_3$, and $MAPbCl_3$ to enhance the d_{33} effective coefficient estimated with the PFM technique, respectively, from 9.7 to 17.9 pm//V, 4.3 to 5.9 pm/V, and 2.7 to 3.4 pm/V. The origin of the piezoelectricity in cubic $MAPbBr_3$ and $MAPbCl_3$ has been attributed to the soft polarity modes and relatively low elastic modulus which modifies the organic–inorganic hydrogen bonding, lattice distortion, and ionic migration. Pb-free $MASnI_3$ films with a d_{33} coefficient of 20 pm/V estimated using the PFM method were reported by Ippili et al., and this is higher than the d_{33}~5pm/V commonly reported for the Pb-containing counterpart $MAPbI_3$ [60]. By regulating the strain in the thin films, a series of $CsPbX_3$ and their mixed halides were explored for their piezoelectric properties by Khan et al. They controlled the halogen atoms (I, Br) in the $CsPbX_3$ (X = Br, Cl) lattice, and intriguing piezoelectric properties of CsPbBr=, $CsPbBr_2I$, $Cs2PbBr_2I_2$, $CsPbI_3$, $CsPbCl_3$, $CsPbCl_2Br$, and $CsPbCl_2I$ were reported. The reported d_{33} values range from 12 pC/N to 47 pC/N. The $CsPbIBr_2$ showed the highest d_{33} coefficient of 47 pC/N, as measured using the vertical-PFM method [61].

Table 2. List of d_{33} coefficients of halide perovskite thin films and the measurement method used. The Curie temperature (T_c) is also included in the case of molecules for which this information was available.

Halide Perovskite Composition	d_{ij} Coefficient (d_{33} Unless Mentioned)	Measurement Method		Reference
$MAPbI_3$	5 pm/N	PFM	58	Ref [55]
Fe: $MAPbI_3$	17.5 pm/N	PFM	~44–47	Ref [56]
$CsPbI_3$	15 pm/N	PFM		Ref [58]
$CsPbBr_3$	23 pm/N	PFM	130	Ref [59]
$MAPbCl_3$	3.4 pm/N	PFM		Ref [62]
$MAPbBr_3$	4.9 pm/N	PFM		Ref [62]
$MASnI_3$	20 pm/V	PFM	30	Ref [60]
$CsPbI_2Br$	47 pm/V	PFM	130	Ref [61]

4.3. Dimensional Tuning of Halide Perovskites and the d_{33} Coefficient

Recently, there has been increased interest in the dimensional tuning of halide perovskites to enhance the d_{33} coefficient [63]. A chiral, one-dimensional perovskite (*R*)-(−)-1-cyclohexylethylammonium)PbI_3 has shown to be piezoelectric and ferroelectric, and a d_{33} value of 36 pm/V was measured, higher than that of the 3D hybrid halide perovskites. Another new one-dimensional $BaNiO_3$-like organic−inorganic hybrid perovskite (thiazolidinium)$CdBr_3$ in bulk pellet form has reported a d_{33} coefficient of 15 pc/N, as measured by the conventional quasi-static method [64]. Nanoparticles of $FASnBr_3$ with an excellent d_{33} coefficient, as measured by PFM, have also recently been reported [65].

In contrast to the conventional oxide perovskites, the poling process is not necessary for halide perovskite-based ferroelectric/piezoelectric materials to induce polarisation, as these materials exhibit a self-poling effect [66]. This implies that the dipoles are orderly arranged during the crystallisation process, as has recently been reported by Tao et al. [48,51,67]. So, poling treatment is not routinely performed in these materials, which is an added advantage as it saves energy input, time, and cost. Based on the studies which have conducted the poling process, the applied poling field ranges from 3 kV/cm to 80 kV/cm [15,56,58,59]. These studies show that the poling process enhances the electrical output from the piezoelectric devices based on halide materials and enhances the d_{33} values. The origin of d_{33}

enhancement is mainly ascribed to the increased BX_6 octahedral distortion in the lattice and the off-centring of the B atoms [58,60,62]. Chen et al. [45] and Khan et al. [61] reported that applying a poling voltage of 3 V and 40 V during the PFM measurement was enough to observe the domain switching during the PFM measurement.

The grain size effect on the piezoelectric properties of halide perovskites has not been exploited in detail so far. However, recently, Khan et al. [61] reported that a large grain size (~ 200 nm) is important for enhanced d_{33} values, and the authors attribute this to the easier displacement of domain walls in larger grains. The grain size information is not reported for all the halide perovskites listed in Tables 1 and 2. However, based on the data available, the grain size of some of the piezoelectric halide perovskites ($CsPbI_3$ [58], $CsPbBr_3$ [59], $MASnI_3$ [60], $CsPbI_2Br$ [61], and MDABCO-$NH4I_3$ [52]) listed in Tables 1 and 2 ranges from 200 to 500 nm.

Regarding the measurement methods of the d_{33} coefficient, a comparison of Tables 1 and 2 shows that the crystal and bulk samples are measured using both the quasi-static and PFM methods. In the case of thin-film samples, mainly the PFM technique is used for d_{33} estimation; however, quasi-static measurements for thin-film piezoelectric materials are emerging, as recently shown by Garcia et al. [68]. Even though the Berlincourt meter is easy to use and fast in obtaining d_{33} values, there are some inherent challenges in using this method for thin-film piezoelectric coefficient measurements. Obtaining homogeneous uniaxial stress on thin films on a thick substrate and the possible interference of the transverse piezoelectric effect are considered the main issues [69]. Also, the static pre-load should be applied carefully since this damages the thin film's electric contacts and the active material itself. Further, because of the simplicity of the set-up, there are several commercial systems without any general standard available, making the external comparisons largely variable and difficult, apart from the relative performance comparison from batch to batch [27]. Similarly, regarding the PFM measurement of thin films, this method mainly measures the d_{33} on a nano–micrometre scale and lacks the overall macroscale information of d_{33}. In the PFM method, in some cases, even non-ferroelectric/non-piezoelectric materials have shown piezoresponse hysteresis loops and a 180° difference in phase due to several alternative mechanisms including charge injection and electrostatic effect, ionic motion, electronic transport, and humidity rather than the intrinsic ferroelectricity of the material. So, PFM results alone are not sufficient in concluding the ferroelectric/piezoelectric nature of the thin films. To overcome these challenges, some modifications of the PFM measurement technique such as the presence of an explicit threshold field as a piece of strong evidence for probing the intrinsic ferroelectricity in thin films are also proposed. Moreover, compared to the Berlincourt method, PFM uses an indirect piezoelectric effect, and the measurement requires complex and high-cost electronics, which should have vibration-free isolation to have stable and reliable d_{33} measurements [70].

Though the Curite temperature is not explicitly described here, the family of halide perovskite materials described in Tables 1 and 2 shows that the T_c for these materials ranges from room temperature to 230 °C. This demonstration of piezoelectric properties at RT and above is particularly useful while designing high-power electronic devices and in the integration of these energy harvesters with disruptive technologies such as the Internet of Things (IoT). It is worth noting that the Curie temperature is relatively lower for halide perovskites compared to conventional oxide perovskites such as PZT (T_c = 350 °C) [71].

5. Other Piezoelectric Factors of Halide Perovskites

This review mainly focuses on the d_{33} coefficient of the halide perovskites. However, in the design of efficient mechanical energy harvesters, other piezoelectric factors also need to be considered. The two other most important factors are (i) the voltage coefficient (g_{33}) and (ii) the electromechanical coupling coefficient k^2, as defined in Section 2. Huang et al. previously reported a voltage coefficient (g_{33}) of 980 × 10^{-3}V.m/N for the vacancy-ordered double perovskite of $TMCM_2SnCl_6$ (where TMCM is trimethylchloromethyl ammonium) [40]. This voltage coefficient is much higher compared to conventional oxide-based

piezoelectrics such as PZT ($20 - 30 \times 10^{-3}$ V·m/N) [72,73]. The two-dimensional halide perovskite of (4-amino tetrahydropyran)$_2$PbBr$_4$ [(ATHP)$_2$PbBr$_4$] crystals, mentioned in Section 4.1, has also been reported to have a high g_{33} of 660×10^{-3} Vm/N. Nanorods of mixed halide composition of the same 2D perovskite [(ATHP)2PbBr$_2$Cl$_2$] have shown an even higher g_{33} coefficient of 900 mVm/N and a d_{33} coefficient of 64.6 pC/N [74]. Using these reported d_{33} and g_{33} coefficients and the elastic Young's modulus of 2D perovskites as ~15 GPa [75], we estimated the electromechanical coupling coefficient (k^2 = dgY) as high as 0.8 for 2D halide perovskites. Following the same strategy, the estimation of k^2 for 3D halide perovskites (e.g., MAPbBr$_3$) gives a value less than 0.1 by taking the d_{33} as 20 pC/N (Table 1), the relative dielectric function as 22 [76], and the elastic modulus as ~20 GPa [75]. These calculations show the very promising potential of low-dimension halide perovskites for efficient mechanical energy harvesting.

Summary: A comparison of the d_{33} values of the halide perovskite crystals and thin films, as listed in Tables 1 and 2, clearly demonstrates the promising potential of halide perovskites for piezoelectric energy harvesting. The reported d_{33} values for some of the thin-film halide perovskites are higher than those of thin-film PZT [69] and the most commonly studied polymer piezoelectric PVDF [77]. The myriad of composition and dimension tuneability in halide perovskites along with simple solution processing and easy amenability to form thin films show the promising future of these molecules in piezoelectric energy harvesting and integration with the IoT as compact, portable, and distributed power sources.

Author Contributions: L.K.J.: Conceptualization, supervision, project administration, funding acquisition, writing-original draft preparation, data curation, writing-review and editing. R.S.M.: Methodology, investigation, formal analysis, resources, data curation, writing—review and editing. J.S.: Methodology, investigation, formal analysis, resources, data curation. All authors have read and agreed to the published version of the manuscript.

Funding: L.K.J. acknowledges funding from UKRI-FLF through MR/T022094/1.

Data Availability Statement: No new data were created or analyzed in this study.

Acknowledgments: L.K.J. acknowledges Chris Bowen, University of Bath, UK for all the very helpful scientific discussion related to ferro-and piezoelectricity. L.K.J. also acknowledges Julia Payne from the School of Chemistry, University of St Andrews, for the crystal structure of 3D halide perovskite shown in Figure 1a.

Conflicts of Interest: The authors declare no conflict of interest.

References

1. Georgiadis, A.; Collado, A.; Tentzeris, M.M. *Energy Harvesting: Technologies, Systems, and Challenges*; Cambridge University Press: Cambridge, UK, 2021; ISBN 9781107039377.
2. Shaikh, F.K.; Zeadally, S. *Energy Harvesting in Wireless Sensor Networks and Internet of Things*; IET Digital library: London, UK, 2021. [CrossRef]
3. Mishu, M.K.; Rokonuzzaman, M.; Pasupuleti, J.; Shakeri, M.; Rahman, K.S.; Hamid, F.A.; Tiong, S.K.; Amin, N. Prospective Efficient Ambient Energy Harvesting Sources for IoT-Equipped Sensor Applications. *Electronics* **2020**, *9*, 1345. [CrossRef]
4. Malaji, P.V.; Ali, S.F.; Litak, G. Energy harvesting: Materials, structures and methods. *Eur. Phys. J. Spec. Top.* **2022**, *231*, 1355–1358. [CrossRef]
5. IEA Net Zero by 2050. A Roadmap for the Global Energy Sector. Available online: https://iea.blob.core.windows.net/assets/7ebafc81-74ed-412b-9c60-5cc32c8396e4/NetZeroby2050-ARoadmapfortheGlobalEnergySector-SummaryforPolicyMakers_CORR.pdf (accessed on 10 March 2024).
6. Toprak, A.; Tigli, O. Piezoelectric energy harvesting: State-of-the-art and challenges. *Appl. Phys. Rev.* **2014**, *1*, 031104. [CrossRef]
7. Chalasani, S.; Conrad, J.M. A survey of energy harvesting sources for embedded systems. In Proceedings of the IEEE SoutheastCon 2008, Huntsville, AL, USA, 3–6 April 2008; pp. 442–447.
8. ARM Predicts 1 Trillion IoT Devices by 2035 with New End-to-End Platform. Available online: https://www.itu.int/hub/2020/04/arm-predicts-1-trillion-iot-devices-by-2035-with-new-end-to-end-platform/ (accessed on 20 April 2024).
9. Pecunia, V.; Occhipinti, L.G.; Hoye, R.L.Z. Emerging Indoor Photovoltaic Technologies for Sustainable Internet of Things. *Adv. Energy Mater.* **2021**, *11*, 2100698. [CrossRef]

10. Pandey, R.; Vats, G.; Yun, J.; Bowen, C.R.; Ho-Baillie, A.W.Y.; Seidel, J.; Butler, K.T.; Seok, S. Il Mutual Insight on Ferroelectrics and Hybrid Halide Perovskites: A Platform for Future Multifunctional Energy Conversion. *Adv. Mater.* **2019**, *31*, 1807376. [CrossRef] [PubMed]
11. Chatterjee, A.; Lobato, C.N.; Zhang, H.; Bergne, A.; Esposito, V.; Yun, S.; Insinga, A.R.; Christensen, D.V.; Imbaquingo, C.; Bjørk, R.; et al. Powering internet-of-things from ambient energy: A review. *J. Phys Energy* **2023**, *5*, 022001. [CrossRef]
12. Liu, X.; Wei, X.; Guo, L.; Liu, Y.; Song, Q.; Jamalipour, A. Turning the Signal Interference into Benefits: Towards Indoor Self-Powered Visible Light Communication for IoT Devices in Industrial Radio-Hostile Environments. *IEEE Access* **2019**, *7*, 24978–24989. [CrossRef]
13. Photovoltaic Technologies Efficiency Charge from 1976 to 2024. Available online: https://www.nrel.gov/pv/cell-efficiency.html (accessed on 20 January 2024).
14. Manzi, M.; Pica, G.; De Bastiani, M.; Kundu, S.; Grancini, G.; Saidaminov, M.I. Ferroelectricity in Hybrid Perovskites. *J. Phys. Chem. Lett.* **2023**, *14*, 3535–3552. [CrossRef] [PubMed]
15. Jella, V.; Ippili, S.; Eom, J.H.; Pammi, S.V.N.; Jung, J.S.; Tran, V.D.; Nguyen, V.H.; Kirakosyan, A.; Yun, S.; Kim, D.; et al. A comprehensive review of flexible piezoelectric generators based on organic-inorganic metal halide perovskites. *Nano Energy* **2019**, *57*, 74–93. [CrossRef]
16. Park, H.; Ha, C.; Lee, J.H. Advances in piezoelectric halide perovskites for energy harvesting applications. *J. Mater. Chem. A* **2020**, *8*, 24353–24367. [CrossRef]
17. Stranks, S.D.; Snaith, H.J. Metal-halide perovskites for photovoltaic and light-emitting devices. *Nat. Nanotechnol.* **2015**, *10*, 391–402. [CrossRef]
18. Park, N.G. Perovskite solar cells: An emerging photovoltaic technology. *Mater. Today* **2015**, *18*, 65–72. [CrossRef]
19. Giorgi, G.; Fujisawa, J.I.; Segawa, H.; Yamashita, K. Organic-Inorganic hybrid lead iodide perovskite featuring zero dipole moment guanidinium cations: A theoretical analysis. *J. Phys. Chem. C* **2015**, *119*, 4694–4701. [CrossRef]
20. Jagadamma, L.K.; Wang, S. Wide-Bandgap Halide Perovskites for Indoor Photovoltaics. *Front. Chem.* **2021**, *9*, 71. [CrossRef]
21. Mao, L.; Stoumpos, C.C.; Kanatzidis, M.G. Two-Dimensional Hybrid Halide Perovskites: Principles and Promises. *J. Am. Chem. Soc.* **2019**, *141*, 1171–1190. [CrossRef] [PubMed]
22. Li, L.; Liu, X.; Li, Y.; Xu, Z.; Wu, Z.; Han, S.; Tao, K.; Hong, M.; Luo, J.; Sun, Z. Two-Dimensional Hybrid Perovskite-Type Ferroelectric for Highly Polarization-Sensitive Shortwave Photodetection. *J. Am. Chem. Soc.* **2019**, *141*, 2623–2629. [CrossRef]
23. Rahmany, S.; Shpatz Dayan, A.; Wierzbowska, M.; Ong, A.J.; Li, Y.; Magdassi, S.; Tok, A.I.Y.; Etgar, L. The Impact of Piezoelectricity in Low Dimensional Metal Halide Perovskite. *ACS Energy Lett.* **2024**, 1527–1536. [CrossRef]
24. Deutz, D.B.; Pascoe, J.-A.; Schelen, B.; van der Zwaag, S.; de Leeuw, D.M.; Groen, P. Analysis and experimental validation of the figure of merit for piezoelectric energy harvesters. *Mater. Horiz.* **2018**, *5*, 444–453. [CrossRef]
25. Jaffe, B.; Cook, W.R.; Jaffe, H. *Chapter 3—Measurement Techniques*; Academic Press: Cambridge, MA, USA, 1971; pp. 23–47. ISBN 978-0-12-379550-2.
26. Li, J. *Lead-Free Piezoelectric Materials*; Springer: Dordrecht, The Netherlands; Heidelberg, Germany; New York, NY, USA; London, UK, 2021; p. 92.
27. Stewart, M.; Cain, M.G. *Characterisation of Ferroelectric Bulk Materials and Thin Films*; Springer: Dordrecht, The Netherlands; Heidelberg, Germany; New York, NY, USA; London, UK, 2014; Volume 2, p. 41.
28. Arnau, A.; Soares, D. *Fundamentals of Piezoelectricity*; Springer: Berlin/Heidelberg, Germany, 2008; pp. 1–38.
29. He, L.; Feng, X.; Triantafillos, K.; Feng, N.; Bo, Z.; Ping, Y. Comparison between methods for the measurement of the D 33 constant of piezoelectric materials. In Proceedings of the 25th International Congress on Sound and Vibration, Hiroshima, Japan, 8–12 July 2018; Volume 1, pp. 77–84.
30. Li, X.; Guo, M.; Dong, S. A flex-compressive-mode piezoelectric transducer for mechanical vibration/strain energy harvesting. *IEEE Trans. Ultrason. Ferroelectr. Freq. Control* **2011**, *58*, 698–703.
31. Available online: https://www.eeict.cz/eeict_download/archiv/sborniky/EEICT_2011_sbornik/03-Doktorske%20projekty/03-Kybernetika%20a%20automatizace/07-xfialk02.pdf (accessed on 2 February 2024).
32. Fialka, J.; Skula, D. *Utilization of the Laser Interferometer for the Measurement of Piezoelectric Charge Constant D_{31} and D_{33}*; Wiley-VCH GmbH: Weinheim/Berlin, Germany, 2011.
33. Fundamentals of Piezoelectricity. In *Lead-Free Piezoelectric Materials*; Wiley-VCH GmbH: Weinheim/Berlin, Germany, 2021; pp. 1–18. ISBN 9783527817047.
34. Seol, D.; Kim, B.; Kim, Y. Non-piezoelectric effects in piezoresponse force microscopy. *Curr. Appl. Phys.* **2017**, *17*, 661–674. [CrossRef]
35. Zhao, X.; Zhang, X.; Zhao, Z.; Wang, Y.; Yin, Y.; Li, X.; Wang, J.; Yuan, G.; Liu, J. Macroscopic piezoelectricity of an MAPbI3 semiconductor and its associated multifunctional device. *Nano Energy* **2023**, *118*, 108980. [CrossRef]
36. Lai, Q.; Zhu, L.; Pang, Y.; Xu, L.; Chen, J.; Ren, Z.; Luo, J.; Wang, L.; Chen, L.; Han, K.; et al. Piezo-phototronic Effect Enhanced Photodetector Based on $CH_3NH_3PbI_3$ Single Crystals. *ACS Nano* **2018**, *12*, 10501–10508. [CrossRef] [PubMed]
37. Ding, Y.; Zhao, X.; Zhao, Z.; Wang, Y.; Wu, T.; Yuan, G.; Liu, J.-M. Strain-Manipulated Photovoltaic and Photoelectric Effects of the $MAPbBr_3$ Single Crystal. *ACS Appl. Mater. Interfaces* **2022**, *14*, 52134–52139. [CrossRef]

38. Zhao, X.; Zhao, Z.; Chai, Y.; Ding, Y.; Li, X.; Yan, Z.; Zhang, X.; Yuan, G.; Liu, J. Macroscopic Piezoelectricity of Halide Perovskite Single Crystals and Their Highly Sensitive Self-Powered X-ray Detectors. *ACS Appl. Mater. Interfaces* **2023**, *15*, 48375–48381. [CrossRef] [PubMed]
39. Ding, Y.; Zhao, X.; Zhao, Z.; Yan, Z.; Yuan, G.; Liu, J.-M. Light and Force Multifunctional Detector Based on the Interfacial Polarization of the ITO/$MAPbBr_3$ Schottky Junction. *Adv. Opt. Mater.* **2024**, *12*, 2301733. [CrossRef]
40. Huang, G.; Khan, A.A.; Rana, M.M.; Xu, C.; Xu, S.; Saritas, R.; Zhang, S.; Abdel-Rahmand, E.; Turban, P.; Ababou-Girard, S.; et al. Achieving Ultrahigh Piezoelectricity in Organic–Inorganic Vacancy-Ordered Halide Double Perovskites for Mechanical Energy Harvesting. *ACS Energy Lett.* **2021**, *6*, 16–23. [CrossRef]
41. Chen, X.-G.; Song, X.-J.; Zhang, Z.-X.; Li, P.-F.; Ge, J.-Z.; Tang, Y.-Y.; Gao, J.-X.; Zhang, W.-Y.; Fu, D.-W.; You, Y.-M.; et al. Two-Dimensional Layered Perovskite Ferroelectric with Giant Piezoelectric Voltage Coefficient. *J. Am. Chem. Soc.* **2020**, *142*, 1077–1082. [CrossRef] [PubMed]
42. Liao, W.-Q.; Zhao, D.; Tang, Y.-Y.; Zhang, Y.; Li, P.-F.; Shi, P.-P.; Chen, X.-G.; You, Y.-M.; Xiong, R.-G. A molecular perovskite solid solution with piezoelectricity stronger than lead zirconate titanate. *Science* **2019**, *363*, 1206–1210. [CrossRef]
43. Rotan, M.; Zhuk, M.; Glaum, J. Activation of ferroelectric implant ceramics by corona discharge poling. *J. Eur. Ceram. Soc.* **2020**, *40*, 5402–5409. [CrossRef]
44. Bagheri, M.H.; Khan, A.A.; Shahzadi, S.; Rana, M.M.; Hasan, M.S.; Ban, D. Advancements and challenges in molecular/hybrid perovskites for piezoelectric nanogenerator application: A comprehensive review. *Nano Energy* **2024**, *120*, 109101. [CrossRef]
45. Chen, X.-G.; Tang, Y.-Y.; Lv, H.-P.; Song, X.-J.; Peng, H.; Yu, H.; Liao, W.-Q.; You, Y.-M.; Xiong, R.-G. Remarkable Enhancement of Piezoelectric Performance by Heavy Halogen Substitution in Hybrid Perovskite Ferroelectrics. *J. Am. Chem. Soc.* **2023**, *145*, 1936–1944. [CrossRef] [PubMed]
46. Yang, C.-K.; Chen, W.-N.; Ding, Y.-T.; Wang, J.; Rao, Y.; Liao, W.-Q.; Tang, Y.-Y.; Li, P.-F.; Wang, Z.-X.; Xiong, R.-G. The First 2D Homochiral Lead Iodide Perovskite Ferroelectrics: [R- and S-1-(4-Chlorophenyl)ethylammonium]$_2PbI_4$. *Adv. Mater.* **2019**, *31*, 1808088. [CrossRef] [PubMed]
47. An, L.-C.; Zhao, C.; Zhao, Y.; Zhang, Y.; Li, K.; Stroppa, A.; Li, W.; Bu, X.-H. Chiral 1D Hybrid Metal Halides with Piezoelectric Energy Harvesting and Sensing Properties. *Small Struct.* **2023**, *4*, 2300135. [CrossRef]
48. Tao, K.; Zhang, B.; Li, Q.; Yan, Q. Centimeter-Sized Piezoelectric Single Crystal of Chiral Bismuth-Based Hybrid Halide with Superior Electrostrictive Coefficient. *Small* **2023**, *19*, 2207663. [CrossRef] [PubMed]
49. Zhang, Y.-Z.; Sun, D.-S.; Gao, J.-X.; Hua, X.-N.; Chen, X.-G.; Mei, G.-Q.; Liao, W.-Q. A Semiconducting Organic–Inorganic Hybrid Perovskite-type Non-ferroelectric Piezoelectric with Excellent Piezoelectricity. *Chem.—An Asian J.* **2019**, *14*, 1028–1033. [CrossRef]
50. Guo, T.-M.; Gong, Y.-J.; Li, Z.-G.; Liu, Y.-M.; Li, W.; Li, Z.-Y.; Bu, X.-H. A New Hybrid Lead-Free Metal Halide Piezoelectric for Energy Harvesting and Human Motion Sensing. *Small* **2022**, *18*, 2103829. [CrossRef] [PubMed]
51. Sahoo, A.; Paul, T.; Makani, N.H.; Maiti, S.; Banerjee, R. High piezoresponse in low-dimensional inorganic halide perovskite for mechanical energy harvesting. *Sustain. Energy Fuels* **2022**, *6*, 4484–4497. [CrossRef]
52. Wu, H.-S.; Wei, S.-M.; Chen, S.-W.; Pan, H.-C.; Pan, W.-P.; Huang, S.-M.; Tsai, M.-L.; Yang, P.-K. Metal-Free Perovskite Piezoelectric Nanogenerators for Human–Machine Interfaces and Self-Powered Electrical Stimulation Applications. *Adv. Sci.* **2022**, *9*, 2105974. [CrossRef] [PubMed]
53. Ippili, S.; Kim, J.H.; Jella, V.; Behera, S.; Vuong, V.H.; Jung, J.S.; Cho, Y.; Ahn, J.; Kim, I.D.; Chang, Y.H.; et al. Halide double perovskite-based efficient mechanical energy harvester and storage devices for self-charging power unit. *Nano Energy* **2023**, *107*, 108148. [CrossRef]
54. Celestine, L.; Zosiamliana, R.; Gurung, S.; Bhandari, S.R.; Laref, A.; Abdullaev, S.; Rai, D.P. A Halide-Based Perovskite $CsGeX_3$ (X = Cl, Br, and I) for Optoelectronic and Piezoelectric Applications. *Adv. Theory Simul.* **2024**, *7*, 2300566. [CrossRef]
55. Coll, M.; Gomez, A.; Mas-Marza, E.; Almora, O.; Garcia-Belmonte, G.; Campoy-Quiles, M.; Bisquert, J. Polarization Switching and Light-Enhanced Piezoelectricity in Lead Halide Perovskites. *J. Phys. Chem. Lett.* **2015**, *6*, 1408–1413. [CrossRef] [PubMed]
56. Ippili, S.; Jella, V.; Kim, J.; Hong, S.; Yoon, S.-G. Enhanced piezoelectric output performance via control of dielectrics in Fe^{2+}-incorporated MAPbI3 perovskite thin films: Flexible piezoelectric generators. *Nano Energy* **2018**, *49*, 247–256. [CrossRef]
57. Song, J.; Xiao, Z.; Chen, B.; Prockish, S.; Chen, X.; Rajapitamahuni, A.; Zhang, L.; Huang, J.; Hong, X. Enhanced Piezoelectric Response in Hybrid Lead Halide Perovskite Thin Films via Interfacing with Ferroelectric $PbZr_{0.2}Ti_{0.8}O_3$. *ACS Appl. Mater. Interfaces* **2018**, *10*, 19218–19225. [CrossRef] [PubMed]
58. Kim, D.B.; Park, K.S.; Park, S.J.; Cho, Y.S. Microampere-level piezoelectric energy generation in Pb-free inorganic halide thin-film multilayers with Cu interlayers. *Nano Energy* **2022**, *92*, 106785. [CrossRef]
59. Kim, D.B.; Park, K.H.; Cho, Y.S. Origin of high piezoelectricity of inorganic halide perovskite thin films and their electromechanical energy-harvesting and physiological current-sensing characteristics. *Energy Environ. Sci.* **2020**, *13*, 2077–2086. [CrossRef]
60. Ippili, S.; Jella, V.; Eom, J.-H.; Kim, J.; Hong, S.; Choi, J.-S.; Tran, V.-D.; Van Hieu, N.; Kim, Y.-J.; Kim, H.-J.; et al. An eco-friendly flexible piezoelectric energy harvester that delivers high output performance is based on lead-free $MASnI_3$ films and $MASnI_3$-PVDF composite films. *Nano Energy* **2019**, *57*, 911–923. [CrossRef]
61. Khan, A.A.; Rana, M.M.; Wang, S.; Fattah, M.F.A.; Kayaharman, M.; Zhang, K.; Benedict, S.; Goldthorpe, I.A.; Zhou, Y.N.; Sargent, E.H.; et al. Control of Halogen Atom in Inorganic Metal-Halide Perovskites Enables Large Piezoelectricity for Electromechanical Energy Generation. *Small* **2023**, *19*, 2303366. [CrossRef] [PubMed]

62. Kim, D.B.; Jo, K.S.; Park, K.S.; Cho, Y.S. Anion-Dependent Polarization and Piezoelectric Power Generation in Hybrid Halide $MAPbX_3$ (X = I, Br, and Cl) Thin Films with Out-of-Plane Structural Adjustments. *Adv. Sci.* **2023**, *10*, 2204462. [CrossRef] [PubMed]
63. Sahoo, S.; Deka, N.; Boomishankar, R. Piezoelectric energy harvesting of a bismuth halide perovskite stabilised by chiral ammonium cations. *CrystEngComm* **2022**, *24*, 6172–6177. [CrossRef]
64. He, L.; Liu, Y.; Shi, P.; Cai, H.; Fu, D.; Ye, Q. Energy Harvesting and Pd(II) Sorption Based on Organic–Inorganic Hybrid Perovskites. *ACS Appl. Mater. Interfaces* **2020**, *12*, 53799–53806. [CrossRef]
65. Rana, M.M.; Khan, A.A.; Zhu, W.; Fattah, M.F.A.; Kokilathasan, S.; Rassel, S.; Bernard, R.; Ababou-Girard, S.; Turban, P.; Xu, S.; et al. Enhanced piezoelectricity in lead-free halide perovskite nanocomposite for self-powered wireless electronics. *Nano Energy* **2022**, *101*, 107631. [CrossRef]
66. Hou, Y.; Wu, C.; Yang, D.; Ye, T.; Honavar, V.G.; van Duin, A.C.T.; Wang, K.; Priya, S. Two-dimensional hybrid organic–inorganic perovskites as emergent ferroelectric materials. *J. Appl. Phys.* **2020**, *128*, 60906. [CrossRef]
67. Pandey, R.; SB, G.; Grover, S.; Singh, S.K.; Kadam, A.; Ogale, S.; Waghmare, U.V.; Rao, V.R.; Kabra, D. Microscopic Origin of Piezoelectricity in Lead-Free Halide Perovskite: Application in Nanogenerator Design. *ACS Energy Lett.* **2019**, *4*, 1004–1011. [CrossRef]
68. Garcia, M.P.; Gibson, D.; Hughes, D.A.; Nuñez, C.G. A Refined Quasi-Static Method for Precise Determination of Piezoelectric Coefficient of Nanostructured Standard and Inclined Thin Films. *Adv. Phys. Res.* **2024**, *3*, 2300091. [CrossRef]
69. Huang, Z.; Zhang, Q.; Corkovic, S.; Dorey, R.; Whatmore, R.W. Comparative measurements of piezoelectric coefficient of PZT films by berlincourt, interferometer, and vibrometer methods. *IEEE Trans. Ultrason. Ferroelectr. Freq. Control* **2006**, *53*, 2287–2293. [CrossRef] [PubMed]
70. Guan, Z.; Jiang, Z.-Z.; Tian, B.-B.; Zhu, Y.-P.; Xiang, P.-H.; Zhong, N.; Duan, C.-G.; Chu, J.-H. Identifying intrinsic ferroelectricity of thin film with piezoresponse force microscopy. *AIP Adv.* **2017**, *7*, 95116. [CrossRef]
71. Shimizu, T.; Katayama, K.; Kiguchi, T.; Akama, A.; Konno, T.J.; Sakata, O.; Funakubo, H. The demonstration of significant ferroelectricity in epitaxial Y-doped HfO_2 film. *Sci. Rep.* **2016**, *6*, 32931. [CrossRef] [PubMed]
72. Zhang, Y.; Roscow, J.; Xie, M.; Bowen, C. High piezoelectric sensitivity and hydrostatic figures of merit in unidirectional porous ferroelectric ceramics fabricated by freeze casting. *J. Eur. Ceram. Soc.* **2018**, *38*, 4203–4211. [CrossRef]
73. Lee, M.K.; Kim, B.H.; Lee, G.J. Piezoelectric voltage constant and sensitivity enhancements through phase boundary structure control of lead-free (K,Na)NbO_3-based ceramics. *J. Eur. Ceram. Soc.* **2022**, *42*, 4898–4906. [CrossRef]
74. Khan, A.A.; Huang, G.; Rana, M.M.; Mei, N.; Biondi, M.; Rassel, S.; Tanguy, N.; Sun, B.; Leonenko, Z.; Yan, N.; et al. Superior transverse piezoelectricity in organic-inorganic hybrid perovskite nanorods for mechanical energy harvesting. *Nano Energy* **2021**, *86*, 106039. [CrossRef]
75. Rathore, S.; Leong, W.L.; Singh, A. Mechanical properties estimation of 2D–3D mixed organic-inorganic perovskites based on methylammonium and phenylethyl-ammonium system using a combined experimental and first-principles approach. *J. Alloys Compd.* **2023**, *936*, 168328. [CrossRef]
76. Govinda, S.; Kore, B.P.; Bokdam, M.; Mahale, P.; Kumar, A.; Pal, S.; Bhattacharyya, B.; Lahnsteiner, J.; Kresse, G.; Franchini, C.; et al. Behavior of Methylammonium Dipoles in $MAPbX_3$ (X = Br and I). *J. Phys. Chem. Lett.* **2017**, *8*, 4113–4121. [CrossRef] [PubMed]
77. Zhang, C.; Wei, W.; Sun, H.; Zhu, Q. Performance enhancements in poly(vinylidene fluoride)-based piezoelectric films prepared by the extrusion-casting process. *J. Mater. Sci. Mater. Electron.* **2021**, *32*, 21837–21847. [CrossRef]